JGR Solid Earth

RESEARCH ARTICLE
10.1029/2022JB025724

This article is a companion to Wiesman et al. (2023), https://doi.org/10.1029/2022JB025723.

Key Points:

- Samples of olivine plus periclase were deformed to high strain to study the effect of the amount of each phase on the mechanical behavior
- Olivine-rich samples undergo strain weakening while ferropericlase-rich samples undergo strain hardening during deformation
- At high strain, all samples are stronger than predicted by flow laws for the constituent phases

Supporting Information:

Supporting Information may be found in the online version of this article.

Correspondence to:

H. S. Wiesman,
hsw42@cam.ac.uk

Citation:

Wiesman, H. S., Zimmerman, M. E., & Kohlstedt, D. L. (2023). The effect of secondary-phase fraction on the deformation of olivine + ferropericlase aggregates: 2. Mechanical behavior. *Journal of Geophysical Research: Solid Earth*, *128*, e2022JB025724. https://doi.org/10.1029/2022JB025724

Received 3 OCT 2022
Accepted 12 MAR 2023

Author Contributions:

Conceptualization: Harison S. Wiesman, Mark E. Zimmerman, David L. Kohlstedt
Data curation: Harison S. Wiesman
Formal analysis: Harison S. Wiesman
Funding acquisition: Mark E. Zimmerman, David L. Kohlstedt
Methodology: Harison S. Wiesman, Mark E. Zimmerman, David L. Kohlstedt
Supervision: Mark E. Zimmerman, David L. Kohlstedt

The Effect of Secondary-Phase Fraction on the Deformation of Olivine + Ferropericlase Aggregates: 2. Mechanical Behavior

Harison S. Wiesman[1,2], Mark E. Zimmerman[3], and David L. Kohlstedt[3]

[1]School of Physics and Astronomy, University of Minnesota-Twin Cities, Minneapolis, MN, USA, [2]Now at Department of Earth Sciences, University of Cambridge, Cambridge, UK, [3]Department of Earth and Environmental Sciences, University of Minnesota-Twin Cities, Minneapolis, MN, USA

Abstract To study the mechanical behavior of polymineralic rocks, we performed deformation experiments on two-phase aggregates of olivine (Ol) + ferropericlase (Per) with periclase fractions (f_{Per}) between 0.1 and 0.8. Each sample was deformed in torsion at $T = 1523$ K, $P = 300$ MPa at a constant strain rate to a final shear strain of $\gamma = 6$ to 7. The stress-strain data and calculated values of the stress exponent, n, indicate that Ol in our samples deformed by dislocation-accommodated sliding along grain interfaces while Per deformed via dislocation creep. At shear strains of $\gamma < 1$, the strengths of samples with $f_{Per} > 0.5$ match model predictions for both phases deforming at the same stress, the lower-strength bound for two-phase materials, while the strengths of samples with $f_{Per} < 0.5$ are greater than predicted by models for both phases deforming at the same strain rate, the upper-strength bound. These observations suggest a transition from a weak-phase supported to a strong-phase supported regime with decreasing f_{Per}. Above $\gamma = 4$, however, the strength of all two-phase samples is greater than those predicted by either the uniform-stress or the uniform-strain rate bound. We hypothesize that the high strengths in the Ol + Per system are due to the presence of phase boundaries in two-phase samples, for which deformation is rate limited by dislocation motion along interfacial boundaries. This observation contrasts with the mechanical behavior of samples consisting of Ol + pyroxene, which are weaker, possibly due to impurities at phase boundaries.

Plain Language Summary If rocks made up of more than one mineral are deformed at high temperatures, their strengths are different than those of each mineral deformed separately. Because rocks at the boundaries between tectonic plates on Earth are, in general, made up of more than one mineral type, this effect is important for understanding the strength of these boundaries. To determine how the amount of each mineral in the rock affects its strength, we performed high-temperature deformation experiments on rocks that contained two mineral types, olivine and periclase. We found that the deformation behavior of the two-phase rock is controlled by the properties of the mineral that makes up most of the rock. After deformation has occurred for a long time, the interaction between the two different minerals that make up our experimental samples can result in the rock being stronger than either mineral by itself.

1. Introduction

The mechanical and microstructural properties of rocks made up of more than one mineral phase differ significantly from those of their single-phase components (Handy, 1990; Herwegh et al., 2011; Ji et al., 2003). These properties are particularly important along shear zones where fine-grained mylonites and ultramylonites are composed of two or more mineral phases that are intimately mixed at the grain scale. Importantly, secondary mineral phases help maintain small grain sizes over prolonged periods of time (Ambrose et al., 2018; Czertowicz et al., 2016; Hansen & Warren, 2015; Linckens et al., 2011; Tasaka et al., 2014; Warren & Hirth, 2006) by hindering grain growth through the process of Zener pinning (Evans et al., 2001; Manohar et al., 1998; Smith, 1948). Pinning then allows for further deformation-driven grain-size reduction, which contributes to strain weakening and localization in these fine-grained regions (Bercovici & Mulyukova, 2018, 2021; Bercovici & Ricard, 2012; Herwegh et al., 2011). Therefore, establishing a thorough understanding of the mechanical behavior and microstructural evolution of polymineralic rocks is important for modeling the geodynamic behavior of shear zones.

Previous studies of two-phase materials combined modeling efforts with experimental studies at small strains ($\gamma < 1$) to examine variations in mechanical behavior associated with different proportions of the two phases (Handy, 1990; Huet et al., 2014; Ji et al., 2003; Tasaka & Hiraga, 2013; Tullis et al., 1991; Wenk et al., 1991).

Writing – original draft: Harison S. Wiesman
Writing – review & editing: Harison S. Wiesman, Mark E. Zimmerman, David L. Kohlstedt

However, shear zones typically experience large strains ($\gamma \gg 1$) for which the mechanical behavior of polymineralic rocks has been less thoroughly studied.

Recent high-strain experimental studies have demonstrated that the mechanical behavior of olivine-bearing rocks depends on the mineralogy of their constituent phases. Tasaka et al. (2017, 2020) determined that two-phase samples of Fe-rich olivine (Ol, Fo_{50}) + orthopyroxene (Opx) deformed to shear strains of $\gamma \leq 25$ were stronger than single-phase samples of Fo_{50} at the beginning of each experiment but weakened continuously such that they were weaker than single-phase Fo_{50} at large strains. Sundberg and Cooper (2008) and Zhao et al. (2019) found that two-phase samples of both Ol (Fo_{92}) + Opx deformed to $\gamma \leq 4$ and of Ol (Fo_{90}) + clinopyroxene (Cpx) deformed to $\gamma \leq 9$ were weaker than the single-phase Ol end-members. Bystricky et al. (2006) determined that two-phase samples of Ol (Fo_{90}) + 80% ferropericlase (Per_{70}) deformed to $\gamma \leq 15$ had a strength similar to that of single-phase Per_{70}. Lastly, Wiesman et al. (2018) observed that two-phase samples of Ol (Fo_{90}) + 30% ferropericlase (Per_{90}) deformed to $\gamma \leq 14$ were stronger than single-phase Ol. Alongside these experimental studies, recent models predict significant weakening at large strains ($\gamma > 10$) due to grain-size reduction resulting from grain-boundary pinning associated with phase mixing (Bercovici et al., 2023).

In the present study, to further characterize the rheological properties of two-phase rocks at large strains, we deformed aggregates of Ol + periclase (Per) to shear strains of $\gamma > 6$. Here, we focus on the mechanical behavior of this two-phase system over a range of secondary-phase fractions from $f_{Per} = 0.1$ to 0.8, while a companion paper focuses on the microstructural evolution in these experiments. Even though Ol and Per do not occur at the same depth in the Earth, both are geologically important materials whose mechanical behaviors have been well characterized. Thus, they provide a valuable system on which to study the physics of deformation of polymineralic materials more generally and with which to reconcile some of the differences between our results and those from the studies listed above. Additionally, depending on Fe content, Per is 2 to 10 times weaker than Ol under our experimental conditions, allowing examination of the effect of a weaker phase on the mechanical properties of Ol.

2. Methods

2.1. Sample Preparation

Details of the sample preparation are provided in our companion paper; thus, only the relevant information is summarized here. Eight two-phase samples were prepared from powders of San Carlos olivine (SC-Ol, Fo_{90}; i.e., $(Mg_{0.9}Fe_{0.1})_2SiO_4$) mixed with powders of either synthetic periclase (Per_{100}; i.e., MgO) or synthetic ferropericlase (Per_{90} or Per_{70}; i.e., $(Mg_{0.9}Fe_{0.1})O$ or $(Mg_{0.7}Fe_{0.3})O$); these included five samples prepared with Per_{100}, one sample prepared with Per_{90}, and two samples prepared with Per_{70}. The phase fraction of each sample is summarized in Table 1.

Powders were uniaxially cold pressed into a Ni can at room temperature with a uniaxial pressure of 100 to 150 MPa. Subsequently, an evacuated hot press was performed in a gas-medium apparatus (Paterson, 1990) at a confining pressure, P, of 300 MPa and a temperature, T, of 1523 K for 2 to 3 hr while a vacuum of 10 to 20 Pa was drawn on one end of the sample. This approach results in greater densification than obtained by conventional hot pressing (Meyers et al., 2017). Initial grain sizes for each of the starting materials are reported in Table 1. After hot pressing, samples were cut into ~3-mm tall cylindrical disks with an outer sample diameter between 11.0 and 12.6 mm for deformation experiments. Some powders were also cold pressed into a Ni can that contained a central Ni post, resulting in thin-walled samples with internal diameter of ~8.0 mm after hot pressing. Thin-walled samples minimize the gradient in stress along the sample diameter. Because Ni is significantly weaker than the thin-walled rock sample (Frost & Ashby, 1982; Hansen et al., 2012; Paterson & Olgaard, 2000), the addition of an internal Ni post introduces only a small correction to the measured torque, which will be further discussed in Section 2.2. The results of microstructural analyses are reported in our companion paper, and relevant parameters, such as grain size, are summarized in Table 1.

2.2. Deformation Experiments

To prepare each deformation assembly, a sample was sandwiched between dunite and porous alumina spacers. Spacers made from discs of Balsam Gap dunite were annealed in a one-atmosphere furnace at $T = 1373$ K and

Table 1
Summary of Mechanical and Microstructural Information for All Deformed Samples

Experiment ID	f_{Per}	Initial d_{Ol} (μm)	d_{Ol} (μm)	Initial d_{Per} (μm)	d_{Per} (μm)	γ	$\dot{\varepsilon}$ ($\times 10^{-5}$ s^{-1})	σ (MPa) $0 < \gamma < 1$	σ (MPa) $\gamma > 4$	n	Q
PT-1324[a]	0.0	4.6	8.4	–	–	5.7	8.1	213.9	136.7	3.1 ± 0.3	–
PT-1425	0.1[b]	4.4	3.9	3.9	2.7	4.9	6.3	272.6	201.3	2.8 ± 0.6, 2.5 ± 0.2	–
PT-1420	0.2[b]	3.6	4.4	3.0	3.5	5.7	9.1	200.9	172.2	3.0 ± 0.3, 3.0 ± 0.8	–
PT-1349	0.2[c]	2.9	2.7	1.6	2.2	6.5	8.6	270.7	237.5	3.0 ± 0.5, 3.0 ± 0.4	–
PT-1455	0.2[c]	2.9	3.9	1.6	2.9	3.0	3.7	116.6	189.7	2.2 ± 0.3	350 ± 33
PT-1219[a]	0.3[d]	7.9	4.8	12.2	8.3	1.0	5.8	264.3	–	2.4 ± 0.3	–
PT-1239[a]	0.3[d]	7.9	3.1	12.2	2.9	7.0	6.9	261.0	178.6	–	–
PT-1250[a]	0.3[d]	7.9	3.5	12.2	3.3	14.2	8.7	244.9	199.2, 119.2	3.1 ± 0.3, 2.0 ± 0.9	–
PT-1283[a]	0.3[d]	7.9	3.2	12.2	3.4	4.0	6.9	247.0	194.5	3.2 ± 1.1, 3.2 ± 0.5	–
PT-1358	0.5[c]	3.3	5.0	2.3	4.9	3.5	8.9	179.8	211.5	3.8 ± 0.5	–
PT-1367	0.5[c]	3.3	2.3	2.3	2.7	6.6	8.5	249.9	221.0	4.2 ± 0.3, 4.1 ± 0.8	–
PT-1461	0.5[c]	3.3	2.1	2.3	2.2	2.7	3.7	141.0	208.9	3.8 ± 0.4	320 ± 60
PT-1416	0.6[c]	3.8	3.1	2.8	3.8	5.1	8.9	170.3	215.1	3.4 ± 0.2	–
PT-1414	0.7[c]	3.7	2.5	2.7	3.7	6.1	8.9	152.1	198.7	3.6 ± 0.1, 4.6 ± 0.4	–
PT-1355	0.8[c]	3.3	1.7	5.2	4.4	6.6	8.7	143.4	212.9	4.3 ± 0.4, 4.3 ± 0.9	–
PT-1457	0.8[c]	3.3	2.1	5.2	5.5	2.9	3.8	195.9	243.9	6.0 ± 0.5	325 ± 33
PT-1362	1.0[c]	–	–	5.3	6.6	2.6	8.6	136.1	162.5	4.0 ± 0.3	–
PT-1463	1.0[c]	–	–	5.3	12.9	0.9	3.6	116.2	133.2	3.5 ± 0.3	–
PT-1465	1.0[c]	–	–	5.3	9.3	5.6	8.2	138.8	154.5	5.1 ± 0.2, 4.9 ± 0.1	380 ± 43

Note. All samples were deformed at $T = 1523$ K and $P = 300$ MPa.
[a]Wiesman et al. (2018). [b]Sample prepared with Per_{70}. [c]Sample prepared with Per_{100}. [d]Sample prepared with Per_{90}.

an oxygen partial pressure, p_{O_2}, of $10^{-5.2}$ Pa for 12 hr to remove any water. Spacers made from discs of porous alumina with ~25% porosity were cored from a plate of Al-25 porous alumina obtained from Alfa Aesar. Spacers were placed above and below each sample, and the stack composed of a sample plus neighboring spacers was inserted into an ~15 mm long Ni sleeve with 14.95-mm outer diameter and 13.55-mm inner diameter. The sample and spacers were placed between alumina and zirconia pistons to center the sample in the hot zone of the furnace in the deformation apparatus. The entire assembly was then inserted into a thin-walled Fe jacket before being placed into the pressure vessel for a deformation experiment.

Samples were deformed in a high-resolution, gas-medium deformation apparatus equipped with a torsion actuator, like that described by Paterson and Olgaard (2000). Experiments were performed at $P = 300$ MPa, $T = 1523$ K at a constant twist rate, while torque and twist were measured with an internal load cell and an external rotary variable differential transformer (RVDT), respectively. These quantities were converted into shear stress, τ, shear strain, γ, and shear strain rate, $\dot{\gamma}$, using the appropriate relationships from Paterson and Olgaard (2000) after subtracting the torque supported by the Fe jacket and Ni capsule using flow laws from Frost and Ashby (1982). This torque correction for the jacket materials is small, typically accounting for <5% of the total torque measured. For samples prepared with an internal Ni post, the torque supported by the Ni post accounts for <2% of the total torque. Additionally, the twist and twist rate were corrected to account for the compliance of the apparatus (Hansen et al., 2012). In this study, samples were deformed at a maximum shear strain rate, $\dot{\gamma}$, between 6.5×10^{-5} and 1.5×10^{-4} s^{-1} at the outermost radius of the sample. Experiments were completed once the desired outer-radius (maximum) shear strain was reached, typically between $\gamma = 1$ and $\gamma = 7$.

Once the torque reached a relatively constant value, strain rate and/or temperature were varied to determine parameters in a flow law of the form

$$\dot{\varepsilon} = A\frac{\sigma^n}{d^p}\exp\left(-\frac{Q}{RT}\right), \quad (1)$$

where $\dot{\varepsilon}$ is the equivalent strain rate, σ is the equivalent stress, d is the grain size, n is the stress exponent, p is the grain size exponent, Q is the activation enthalpy, R is the ideal gas constant, and A is a preexponential function that depends on experimental conditions and material parameters, such as water content, melt fraction, p_{O_2}, and shear modulus. A is treated as constant for each experiment in this study. Equivalent stress and strain are related to their shear counterparts using the relations $\sigma = \sqrt{3}\tau$ and $\varepsilon = \frac{\gamma}{\sqrt{3}}$ for the torsion geometry (Paterson & Olgaard, 2000). To calculate n in Equation 1, $\dot{\gamma}$ was varied between 6×10^{-5} and 4×10^{-4} s^{-1} to determine the response in τ while minimizing changes in d and keeping T constant. The strain rate was held constant for strain intervals of $\Delta\gamma \leq 0.1$, at which point the stress had reached a new steady-state value. The strain rate was returned to its original value between rate steps to minimize microstructural changes. Similarly, to calculate Q in Equation 1, T was varied in increments of $\Delta T = 50$ K between 1473 and 1573 K to measure changes in τ while minimizing changes in d and keeping $\dot{\gamma}$ constant. Temperature was held at each value for strain intervals of $\Delta\gamma = 0.1$ to 0.15, typically corresponding to about 30 min, to ensure that stress had reached a new steady-state value. Similar to the procedure used for the rate steps, temperature was returned to the starting temperature of 1523 K between temperature steps to minimize microstructural changes that may occur at different temperatures.

2.3. Microstructural and Chemical Analyses

Results from microstructural analyses, including electron backscatter diffraction (EBSD) analysis, are presented in our companion paper. Chemical analyses via wavelength dispersive spectroscopy (WDS) were also carried out to determine the Fe-Mg contents of both phases in our samples. WDS analyses were conducted using a JEOL JXA-8530FPlus electron probe microanalyzer at an accelerating voltage of 15 kV and beam current of 20 nA, the results of which are presented in Tables S1 and S2 in Supporting Information S1.

3. Results

3.1. Mechanical Data

Shear stress versus shear strain data from each of the deformation experiments conducted at a constant shear strain rate of $\dot{\gamma} = 1.2 \times 10^{-4}$ to 1.5×10^{-4} s^{-1} are plotted in Figure 1. For samples with Per fraction of $f_{Per} > 0.5$, the shear stress increases rapidly upon loading up to ~75 MPa as the sample begins to deform, followed by a continued increase in stress due to rapid work hardening up to $\gamma = 0.1$ (Figures 1a–1d). Above $\gamma = 0.1$ in the two-phase samples, work hardening continues at a slower rate, manifesting as a slower rate of stress increase until the end of the experiment (Figures 1b–1d), while in the single-phase samples, stress remains constant with increasing strain (Figure 1a). For samples with $f_{Per} < 0.5$, stress increases rapidly up to a peak stress at $\gamma = 0.1$–0.7, as demonstrated in Figures 1e–1i. As a sample continues deforming, it either undergoes a 20 to 40 MPa decrease in τ over $\Delta\gamma = 2$ to 4 before reaching a steady-state stress, or it continues to weaken slowly for the duration of the experiment.

In Figure 2, shear stress is plotted as a function of shear strain for experiments conducted at $\dot{\gamma} = 6.5 \times 10^{-5}$ s^{-1}. At this slower strain rate, all samples display similar mechanical behavior with stress increasing rapidly up to $\gamma = 0.1$ to 0.5, then increasing at a slower rate until the experiment was stopped.

Steps in stress that appear in many of the stress-strain curves in Figures 1 and 2 result from stepwise changes in strain rate or temperature, yielding the data used to calculate the stress exponent or activation energy, respectively. Stress exponents were calculated from the slope of a linear least-squares fit to log-log plots of strain rate-torque data obtained from each group of rate steps for each experiment (Figure S1 in Supporting Information S1). For some experiments in Figure 1, two groups of rate steps were performed, each at a different finite strain. In these cases, data from each group of rate steps were fit separately. Values for the stress exponent are presented in Table 1 and plotted versus f_{Per} in Figure 3. For samples with $f_{Per} < 0.5$, stress exponents lie between $n = 2.0$ and 3.2, while for those with $f_{Per} > 0.5$, n typically lies between 3.5 and 5.1; note that, for two of the three samples with $f_{Per} = 0.8$, $n \geq 6$. Values for the activation energy were calculated from the slope of a linear least-squares fit to Arrhenius plots of torque-temperature data for each group of temperature steps (Figure S2 in Supporting Information S1), the results of which are summarized in Table 1 and plotted as a function of f_{Per} in Figure 4. For two-phase samples, Q lies between 320 and 350 kJ/mol, while for the single-phase Per_{100} sample, $Q_{Per} = 380$ kJ/mol. Note that temperature steps were only performed for sample PT-1465 in Figure 1a, and samples PT-1455, PT-1457, and PT-1461 in Figure 2. The stepwise changes in stress corresponding to each group of temperature steps are indicated on their respective figures to help differentiate them from rate steps.

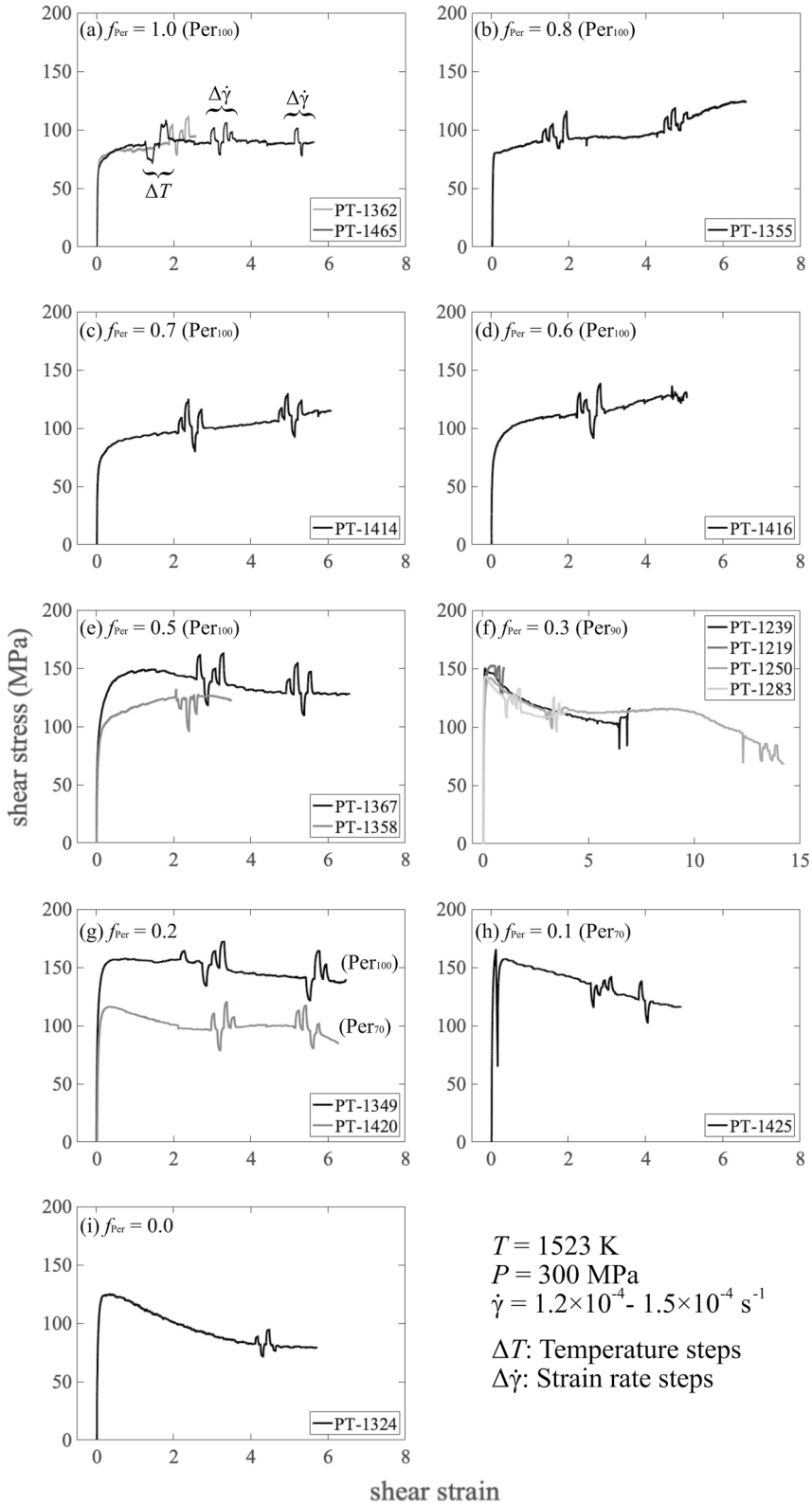
(a) f_{Per} = 1.0 (Per100)
$\Delta\dot{\gamma}$
$\Delta\dot{\gamma}$
ΔT
PT-1362
PT-1465
(b) f_{Per} = 0.8 (Per100)
PT-1355
(c) f_{Per} = 0.7 (Per100)
PT-1414
(d) f_{Per} = 0.6 (Per100)
PT-1416
(e) f_{Per} = 0.5 (Per100)
PT-1367
PT-1358
(f) f_{Per} = 0.3 (Per90)
PT-1239
PT-1219
PT-1250
PT-1283
(g) f_{Per} = 0.2
(Per100)
(Per70)
PT-1349
PT-1420
(h) f_{Per} = 0.1 (Per70)
PT-1425
(i) f_{Per} = 0.0
PT-1324
shear stress (MPa)
shear strain
T = 1523 K
P = 300 MPa
$\dot{\gamma}$ = 1.2×10^{-4}- 1.5×10^{-4} s^{-1}
ΔT: Temperature steps
$\Delta\dot{\gamma}$: Strain rate steps

Figure 1.

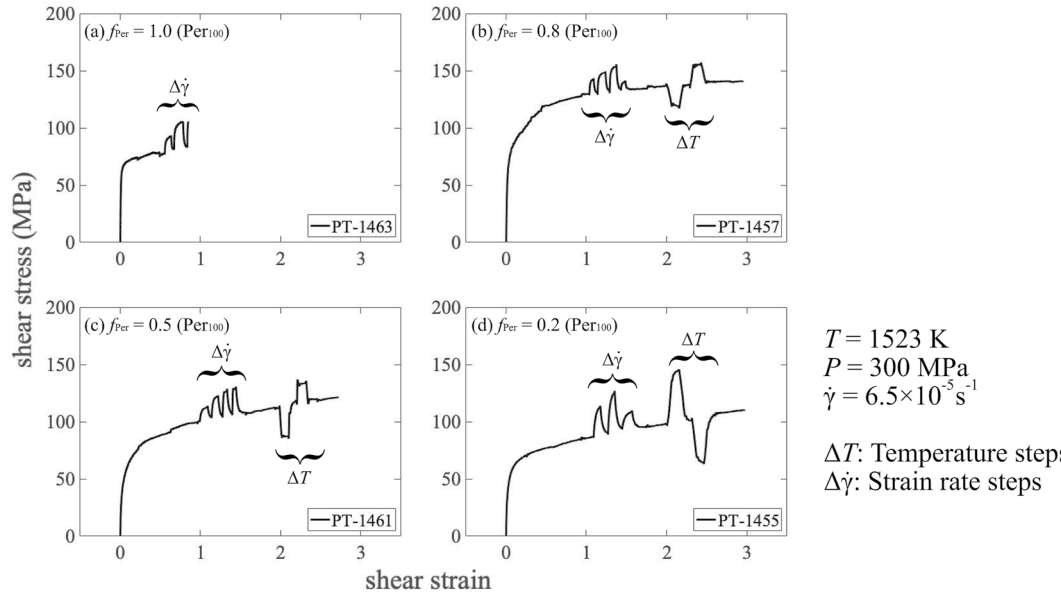

Figure 2. Shear stress versus shear strain data for single-phase and two-phase samples of Ol and Per deformed in torsion with Per fractions of (a) $f_{Per} = 1.0$, (b) $f_{Per} = 0.8$, (c) $f_{Per} = 0.5$, and (d) $f_{Per} = 0.2$. Experiments were performed at $T = 1523$ K, $P = 300$ MPa, and an outer-radius shear strain rate of $\dot{\gamma} \approx 6.5 \times 10^{-5}$ s^{-1}. Strain rate and temperature steps appear as steps in stress along the curves and are noted along each curve.

3.2. Evolution of Fe Contents in Olivine and Periclase

The Fe content in SC-Ol (Fo_{90}) is in equilibrium with Per_{70}, however, the starting materials for samples with $f_{Per} = 0.2$, 0.5, 0.6, 0.7, and 0.8 were synthesized with Per_{100}, and the samples with $f_{Per} = 0.3$ were synthesized using Per_{90} as the second phase. Therefore, in these samples, Fe was lost from SC-Ol to Per via diffusion during hot pressing. As discussed in our companion paper, these experiments were originally designed to examine the physical processes responsible for phase mixing (Wiesman et al., 2018), in which case the Fe content should not be a concern. To confirm this expectation, we prepared two samples with Per_{70} (PT-1420 and PT-1425).

Select samples were analyzed via WDS and the Fe-Mg contents of these samples are summarized in Tables S1 and S2 in Supporting Information S1 for Ol and Per in each sample, respectively. This analysis determined that in samples PT-1355, with $f_{Per} = 0.8$, and PT-1349, with $f_{Per} = 0.2$, the composition of Ol evolved from Fo_{90} to Fo_{97} and Fo_{95}, respectively, while the composition of Per evolved from Per_{100} to Per_{99} and Per_{88}, respectively. A similar analysis on sample PT-1239 with $f_{Per} = 0.3$ yielded an Ol composition that evolved from Fo_{90} to Fo_{95} and a Per composition that evolved from Per_{90} to Per_{80}. Therefore, in our two-phase samples, Ol composition is expected to lie in the range Fo_{95} to Fo_{97} and Per composition in the range Per_{80} to Per_{99}. No exchange of Fe between Ol and Per was measured in samples PT-1420 with $f_{Per} = 0.2$ and PT-1425 with $f_{Per} = 0.1$ as they were prepared with Per_{70}.

To demonstrate that the Fe-Mg contents of our samples had finished evolving prior to deformation experiments, we also conducted an WDS analysis on an undeformed sample, PT-1322, the results of which are likewise presented in Tables S1 and S2 in Supporting Information S1. This sample, which was prepared with Per_{100} and contained $f_{Per} = 0.2$, was from the same hot press as sample PT-1349. The composition of Ol and Per measured in this sample revealed that Ol evolved from Fo_{90} to Fo_{95} and Per evolved from Per_{100} to Per_{88}, the same as that in the deformed sample from the same hot press. Therefore, we conclude that Fe-Mg exchange was completed during sample preparation and hot pressing, prior to the deformation experiments.

Figure 1. Shear stress versus shear strain data for single-phase and two-phase samples of Ol and Per deformed in torsion with Per fractions of (a) $f_{Per} = 1.0$, (b) $f_{Per} = 0.8$, (c) $f_{Per} = 0.7$, (d) $f_{Per} = 0.6$, (e) $f_{Per} = 0.5$, (f) $f_{Per} = 0.3$, (g) $f_{Per} = 0.2$, (h) $f_{Per} = 0.1$, and (i) $f_{Per} = 0.0$. Experiments were performed at $T = 1523$ K, $P = 300$ MPa, and an outer-radius shear strain rate of $\dot{\gamma} = 1.2 \times 10^{-4}$ to 1.5×10^{-4} s^{-1}. The composition of Per used in each experiment is noted in each panel. Strain rate and temperature steps appear as steps in stress in the curves. Unless otherwise noted, steps in each of the curves are strain-rate steps; in other words, temperature steps only appear in (a). Data for $f_{Per} = 0.3$ and $f_{Per} = 0.0$ in (f) and (i) are reanalyzed results from Wiesman et al. (2018).

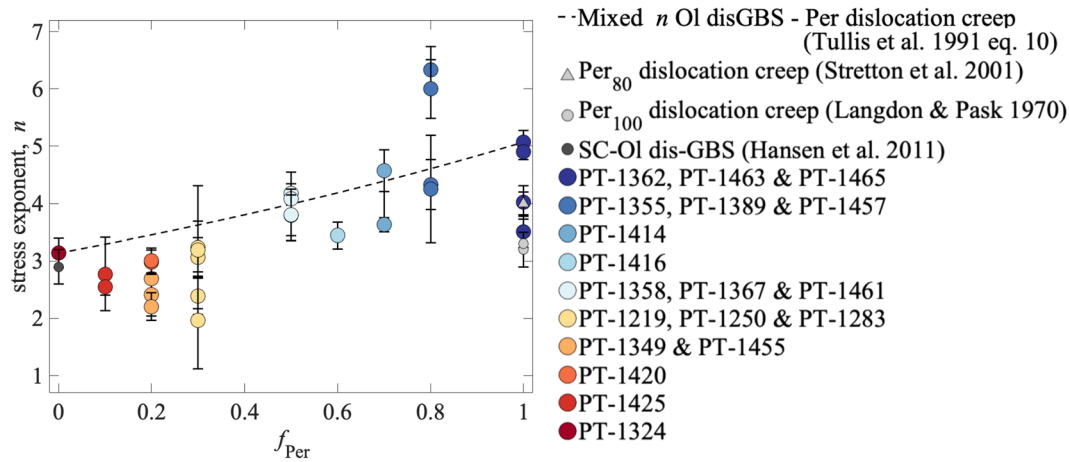

Figure 3. Stress exponent versus f_{Per} for each group of rate steps in each experiment. For each value of n, error bars are the standard error determined from the fit. Values of n are also displayed for disGBS (dark-gray circle) in single-phase Ol determined by Hansen et al. (2011) and for dislocation creep in single-phase Per_{100} (light-gray circles) and Per_{80} (light-gray triangle) determined by Langdon and Pask (1970) and Stretton et al. (2001), respectively. The black dashed line, which is the predictive model for n in two-phase mixtures proposed by Tullis et al. (1991), was calculated based on the values of n from the single-phase end-members for their dominant deformation mechanisms.

4. Discussion

4.1. Considerations for Interpreting the Mechanical Behavior

In the following sections, we discuss several observations and complications that are important to consider when interpreting the mechanical behavior of our samples. These include the microstructural evolution of our samples discussed in our companion paper, the effect of Fe on the mechanical behavior of our samples, strain weakening due to the development of a CPO in our samples, and the effect of silica activity on sample strength due to our use of Per as a secondary phase.

4.1.1. Summary of Important Microstructural Features

In this section, we summarize the results from our companion paper on the microstructural evolution in our samples to help interpret the mechanical data in the following sections.

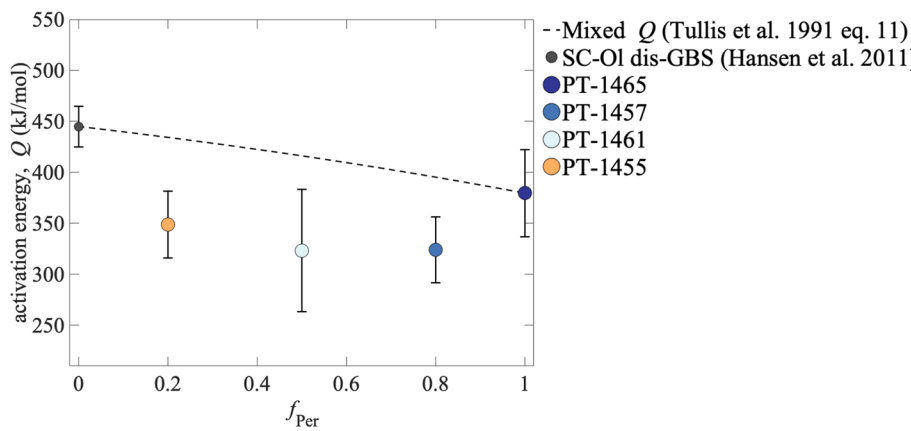

Figure 4. Activation energy versus f_{Per} for each group of temperature steps in each experiment. For each value of Q, error bars are the standard error determined from the fit. The value of Q determined for disGBS in single-phase Ol by Hansen et al. (2011) is plotted for comparison with two-phase samples. The black dashed line, which is from the predictive model for Q in two-phase mixtures proposed by Tullis et al. (1991), was calculated using the value of Q for disGBS in single-phase Ol (Hansen et al., 2011) and the value of Q determined for deformation of single-phase Per_{100} in this study.

The mean grain size of Ol and Per in our two-phase samples either remained the same or decreased slightly during deformation up to $\gamma = 7.0$; the grain size of Ol evolved from 2.9–3.8 to 1.7–4.4 μm during deformation, while the grain size of Per evolved from 1.6–5.2 to 2.2–4.4 μm (Table 1). The mean grain size of Ol tended to decrease with increasing f_{Per} in our two-phase samples, while the mean grain size of Per tended to increase with increasing f_{Per}. These observations contrast with the behavior of our single-phase samples of Ol and Per for which the grain size approximately doubled from 4.6 to 8.4 and 5.3 to 9.2 μm, respectively, during deformation to $\gamma \approx 7.0$. For each two-phase sample, grain sizes of Ol and Per are 2 to 5 times smaller than predicted by a grain-size piezometer calibrated for single-phase samples (companion paper, Figure 10). Additionally, subgrain sizes measured for Ol in our two-phase samples are smaller than predicted by the subgrain-size piezometer from Goddard et al. (2020), likely because the grain size in Ol is smaller than the predicted subgrain size (companion paper, Figure 11). The subgrain size of Per, however, matches the subgrain size predicted by their piezometer within error.

During deformation of two-phase samples, grains of the two phases mixed with one another, resulting in a change in the proportion of Ol-Per phase boundaries and Ol-Ol or Per-Per grain boundaries. We observed that the fraction of phase boundary length out of the total length of grain and phase boundaries evolved to a binomial distribution, which describes a random distribution of the two phases (companion paper, Figure 9).

Deformation resulted in the development of a crystallographic preferred orientation (CPO) of both Ol and Per grains in our samples. Our single-phase sample of Ol developed a relatively strong fabric with [100] maxima in the shear direction and girdles between the [010] and [001] axes, indicating activity of the (010)[100] and (001)[100] slip systems. In our two-phase samples, Ol grains developed a weak fabric corresponding to dislocation activity on the (010)[100] slip system with a set of secondary maxima indicating activity of the (100)[001] slip system as well (companion paper, Figure 6). Our single-phase samples of Per developed a multimaxima pattern, which we interpreted as deformation dominated by dislocation activity on the $\{111\}\langle\bar{1}10\rangle$ family of slip systems as well as the $\{100\}\langle011\rangle$ family of slip systems. In our two-phase samples, Per developed a CPO similar to that in the single-phase sample, which weakened with decreasing f_{Per} (companion paper, Figure 7).

4.1.2. Complications Due To Fe-Mg Exchange

In Section 3.2, we noted differences in the Fe-Mg contents of Ol and Per amongst our two-phase samples. These differences in Fe content can potentially affect the mechanical behavior and microstructural evolution of both phases. For Ol, these effects have been studied in detail by Zhao et al. (2009) and Qi et al. (2021), who determined that Fe concentration affects the strength of Ol independent of microstructural or chemical parameters, such as grain size or water content. Their results allow us to scale flow laws determined for Fo_{90} to the appropriate Fe contents to compare results amongst our samples. Although the effect of Fe on the mechanical behavior of Per has not been studied directly, we can infer this effect using data for Per_{60} from Heidelbach et al. (2009), data for Per_{70} from Bystricky et al. (2006), and the dislocation creep flow law for Per_{80} from Stretton et al. (2001). We can use this collection of results to scale the Per_{80} dislocation creep flow law from Stretton et al. (2001) to different Fe contents, facilitating comparison amongst our samples.

For the range of Fe contents present in Ol in our samples, applying the results of Zhao et al. (2009) and Qi et al. (2021) to modify the dislocation-accommodated grain-boundary sliding (disGBS) flow law for Fo_{90} from Hansen et al. (2011) yields an increase in the strength determined for Fo_{90} by a factor of 1.3 to 1.6 for Fo_{95} and Fo_{97}, respectively. Furthermore, applying our estimate of the effect of Fe on the strength of Per yields strengths that differ by factors of 0.7 and 3.2 from that of Per_{80} (Stretton et al., 2001) for Per_{70} and Per_{99}, respectively. The implications of these differences in Fe content will be further discussed in Section 4.3.

4.1.3. Geometric Softening Due To CPO Development

Hansen et al. (2012) reported strain weakening (geometric softening) by a factor of 0.72 from peak to steady-state stress due to the development of a CPO in their samples of single-phase Fo_{50}. Similar weakening likely occurred for the single-phase Ol sample in this study, as will be discussed in Section 4.2.2. In contrast, the weak CPOs developed for Ol in our two-phase samples indicate that Ol in these samples did not experience significant geometric softening. Therefore, we did not consider geometric softening in our analysis of the mechanical behavior for our two-phase samples.

Despite the formation of a CPO in our sheared single-phase samples of Per_{100}, our samples did not undergo geometric softening (e.g., Figure 1a). In principle, it is possible that geometric softening did occur and was

counteracted by, e.g., strengthening due to grain growth (Table 1). However, stress-strain behavior similar to ours with no strain weakening was observed by Heidelbach et al. (2003) in their high-strain torsion experiments on Per_{80}, despite a reduction in grain size by a factor of 5 (from 40 to 8 μm) and noticeable CPO development. Therefore, we will not consider geometrical softening of Per in the discussion in the following sections. The lack of geometric softening may be due to the availability of more than enough slip systems in face-centered cubic materials such as MgO to easily fulfill the von Mises criterion (von Mises, 1913).

4.1.4. Effect Silica Activity on Sample Strength

Previous studies have demonstrated that the strength of Ol depends on silica activity. Specifically, Ol single crystals buffered by Per are stronger than those buffered by Opx in the dislocation creep regime (Bai et al., 1991; Ricoult & Kohlstedt, 1985). Additionally, in the diffusion creep regime, polycrystalline samples of Fo_{100} + 10% Per_{100} (Okamoto & Hiraga, 2022) are approximately an order of magnitude stronger than samples of Fo_{100} + 20% En_{100} (Nakakoji et al., 2018). To test the effect of silica activity on the strength of our samples deforming in the dislocation-accommodated grain-boundary sliding creep (disGBS) regime, an additional experiment was conducted on a sample of Ol + <10% Per_{70} that yielded a strength within error of, if not slightly weaker than, that predicted by the disGBS flow law determined by Hansen et al. (2011) on SC-Ol containing <5% Opx (Figure S4 in Supporting Information S1). Given this observation, we do not anticipate an effect of silica activity on the strength of our two-phase samples of Ol with significant amounts of Per deformed in the disGBS regime.

4.2. Deformation Mechanisms

To determine the dominant deformation mechanisms for Ol and Per in our samples, the mechanical and microstructural data for our single-phase and two-phase samples are further examined below. Due to the distinction in the mechanical behavior between Ol-rich ($f_{Per} < 0.5$) samples and Per-rich ($f_{Per} > 0.5$) samples noted in Section 3.1, these two domains are considered separately when interpreting the mechanical behavior for samples with $f_{Per} < 0.5$ in Sections 4.2.1 and 4.2.2 and samples with $f_{Per} > 0.5$ Sections 4.2.3 and 4.2.4, respectively. Importantly, this distinction implies that Ol controls the deformation behavior of samples with $f_{Per} < 0.5$ and Per controls the deformation behavior of samples with $f_{Per} > 0.5$.

4.2.1. Deformation Mechanism of Olivine-Rich Samples

The dominant deformation mechanism for Ol in our single-phase and two-phase samples was dislocation-accommodated interface sliding, i.e., disGBS in single-phase Ol and dislocation creep accommodated by sliding along grain and phase boundaries in two-phase samples. Specifically, Ol deformed via dislocation-accommodated interface sliding in the regime for which the grain size is smaller than the subgrain size. This conclusion is supported by the value of the stress exponent, $n = 2.0$ to 3.2, for samples with $f_{Per} < 0.5$ and the observation that grain sizes were smaller than the subgrain size (companion paper, Figure 11). A comparison with results from previous experiments on single-phase Ol and Ol + Opx deformed under similar conditions helps support the interpretation that deformation of Ol was dominated by dislocation-accommodated interface sliding in this study. Both low-strain compression and high-strain torsion experiments performed on SC-Ol and Fo_{50} reported a non-Newtonian stress dependence ($n = 3.4 \pm 0.2, 2.9 \pm 0.3, 4.1 \pm 0.1$) and nonzero grain size sensitivity ($p = 2.0 \pm 0.2, 0.7 \pm 0.1, 0.73 \pm 0.06$) (Hansen et al., 2011, 2012; Wang et al., 2010), while recent studies on two-phase samples of Fe-rich Ol + Opx with $f_{Opx} < 0.5$ reported values for the stress exponent that decreased from $n = 3.0$ to 1.8 with increasing strain and a grain size exponent that simultaneously increased from $p = 1.1$ to 3.3 (Tasaka et al., 2017, 2020). Such values for the stress exponent and grain size exponent are characteristic of models for disGBS, which predict values of $n = 3$, $p = 1$ or $n = 2$, $p = 2$ for materials with grain size greater than or smaller than the subgrain size (Langdon, 2006), respectively; these values are similar to those for n calculated in the present study for samples with $f_{Per} < 0.5$. Additionally, high-strain experiments using both single-phase samples of Fo_{50} (Hansen et al., 2012) and two-phase samples of Fo_{50} + iron-rich enstatite (En_{55}) (Tasaka et al., 2017, 2020) reported mechanical behavior for which a peak stress is reached at $\gamma < 1$, followed by weakening with increasing strain, i.e., a behavior similar to that described for our samples with $f_{Per} < 0.5$ in the present study (Figures 1e–1i). These authors attributed the observed strain weakening to a combination of grain-size reduction and geometric softening.

Finally, in samples with large Per fractions ($f_{Per} > 0.5$), diffusion creep may have contributed as much as ~10% to the deformation of Ol, consistent with the small grain size of Ol in these samples. However, the mechanical behavior of these samples was dominated by Per, as will be discussed further in Section 4.2.3.

4.2.2. Mechanical Behavior of Olivine-Rich Samples

Based on the conclusion that our samples with $f_{Per} < 0.5$ deformed by dislocation-accommodated interface sliding, we further examine the specific behavior of the stress versus strain curves in Figures 1e–1i. Our single-phase SC-Ol sample, PT-1324, strain weakened even though the grain size increased from $d_{Ol} = 4.6$ to 8.4 μm. Based on the disGBS flow law for Ol from Hansen et al. (2011), such an increase in grain size would cause an increase in sample strength of ∼15%. Therefore, a 45% decrease in strength due to the development a strong CPO (companion paper, Figure 6) is required to account for both the increase in stress due to grain growth and the strain weakening observed in Figure 1i. This behavior corresponds to a geometrical softening factor of 0.55 in our single-phase SC-Ol sample, which is about twice that calculated by Hansen et al. (2012) for their experiments on Fo_{50}. Additionally, in Figures 1e–1h, we observed less pronounced strain weakening in our two-phase samples with $f_{Per} < 0.5$ than in the single-phase Ol sample, consistent with the weak CPO development (companion paper, Figure 6) and small amounts of grain-size reduction in our two-phase samples (Table 1).

In contrast to the behavior of samples deformed at faster strain rates, sample PT-1455 with $f_{Per} = 0.2$, which was deformed at half the strain rate as the samples discussed previously ($\dot{\gamma} = 6.5 \times 10^{-5}\ s^{-1}$), hardened over the course of the entire experiment (Figure 2d). This strengthening from 70 MPa at $\gamma = 0.1$ to 110 MPa at $\gamma = 3.0$ is consistent with the observed increase in grain size from 2.9 to 3.9 μm. Based on Equation 1 with $n = 2.2$, we calculate that a grain size exponent of $p = 3.5$ is required to explain the observed strengthening. This value is similar to that of $p = 3.3 \pm 0.7$ reported by Tasaka et al. (2017) at high strains from their experiments on two-phase samples. These authors interpreted their results in terms of disGBS occurring in the regime in which grain size is smaller than subgrain size, which we conclude is the mechanism dominating deformation in experiment PT-1455.

4.2.3. Deformation Mechanism of Ferropericlase-Rich Samples

Based on the deformation behavior of our single-phase Per and Per-rich two-phase samples, we conclude that Per deformed by dislocation creep in our samples. The primary evidence for this conclusion is the relatively large values for the stress exponent of $n = 3.5$ to 5.1 for samples with $f_{Per} > 0.5$. Additionally, above shear strains of $\gamma > 1$, no change in strength with increasing strain occurred in our single-phase Per_{100} samples (Figure 1a), despite an increase from 5.3 to 9.3 μm in the size of Per grains in sample PT-1465 and from 5.3 to 6.6 μm in sample PT-1362 (Table 1). The fact that the same stress was recorded for deformation of multiple samples with different grain sizes, all deformed at the same strain rate, indicates that our single-phase sample of Per_{100} deformed by a grain size-insensitive mechanism, i.e., dislocation creep. A fit to stress versus temperature and strain rate versus stress data in Figure S3 in Supporting Information S1 for our three experiments (PT-1362, PT-1463, and PT-1465) on single-phase Per_{100} yields the following flow law:

$$\dot{\varepsilon} = \left(0.15\ s^{-1} MPa^{-4.4}\right) * \sigma^{4.4 \pm 0.3} \exp\left(\frac{-380 \pm 40\ \frac{kJ}{mol}}{RT}\right). \quad (2)$$

For comparison, previous studies have reported stress exponents of $n = 3.3$, 3.2 ± 0.3, 4.0 ± 0.2, 3.6 ± 0.2 for Per_{100} and Per_{80} (Bilde-Sörensen, 1972; Heidelbach et al., 2003; Langdon & Pask, 1970; Stretton et al., 2001); each of these authors concluded that their samples deformed via dislocation creep. As mentioned previously, values of n in our study lie in the range from 3.5 to 5.1 for samples with $f_{Per} > 0.5$, similar to or larger than previously determined values. Furthermore, in our companion paper, we demonstrated that the subgrain size of Per in our two-phase samples matched that predicted by the subgrain-size piezometer of Goddard et al. (2020), providing additional evidence for dislocation activity resulting in the creation of subgrain boundaries. In samples with $f_{Per} < 0.5$ discussed above in Section 4.2.1, a grain-size sensitive deformation mechanism, such as disGBS or diffusion creep, may have started to contribute to deformation of Per, consistent with the small size of Per grains and the weak CPOs for Per in these samples (see companion paper).

4.2.4. Mechanical Behavior of Ferropericlase-Rich Samples

Based on the conclusion that dislocation creep of Per dominates deformation in our samples with $f_{Per} > 0.5$, we examine the mechanical behavior of these samples in more detail. As described in Section 3.1, the strength of two-phase samples in this study with $f_{Per} > 0.5$ increases with increasing strain over the duration of the experiment (Figures 1b–1d). Insight into possible mechanisms responsible for strain hardening in Per comes from a comparison to the strain hardening behavior of face-centered cubic metals (e.g., Cu, Ni, and Al) deformed in

torsion to strains of $\gamma > 4$ (Rollet et al., 1988; Rollett & Kocks, 1993; Zehetbauer, 2000; Zehetbauer et al., 2003). These authors argued that strain hardening in their samples was controlled by reduction of the mean free path of dislocations with increasing strain, referred to as stage-IV hardening. Explanations for a decrease in the mobility of dislocations with increasing strain are based on either the interaction of dislocations with immobile dislocation debris (Rollett & Kocks, 1993) or the buildup of dislocation pileups at grain/subgrain boundaries that limit dislocation motion (Zehetbauer, 2000). Because strain hardening is not observed during deformation of our single-phase samples of Per_{100}, phase boundaries must play an important role in this hardening processes, possibly by acting as barriers to dislocation recovery and thus facilitating dislocation pileups that restrict dislocation motion.

4.2.5. Activation Energy

While activation energy is often used as an additional constraint on the identity of the dominant deformation mechanism, it is not a highly useful indicator of the deformation mechanism for the two-phase samples in this study given the significant differences between values of Q determined by different researchers for the same deformation mechanism both in Ol and in Per. As displayed in Figure 4, the activation energies calculated for our two-phase samples lie between 300 and 350 kJ/mol. These values of Q are within error of $Q = 327$ kJ/mol determined for dislocation creep in Per_{80} by Stretton et al. (2001); however, values of activation energy determined for dislocation creep of Per_{100} spans the range 210 to 440 kJ/mol (Bilde-Sörensen, 1972; Hensler & Cullen, 1968; Langdon & Pask, 1970). For Ol, the activation energy determined for dislocation-accommodated grain-boundary sliding in SC-Ol of 445 kJ/mol (Hansen et al., 2011) is greater than that determined for two-phase samples in this study. Although the value of $Q = 375$ kJ/mol reported by Hirth and Kohlstedt (2003) for diffusion creep of SC-Ol is closer to the values calculated for our two-phase samples, the more recently determined value of $Q \approx 435$ kJ/mol from Yabe and Hiraga (2020) for diffusion creep in Fo_{90} after accounting for the effect of impurities at our experimental conditions suggests that this comparison may not be useful either.

4.3. Two-Phase Flow

Analysis of the deformation behavior of two-phase materials is made difficult by the complex distribution of stress and strain rate between the two phases. The strength of two-phase materials is often characterized by a rule of mixtures that combines flow laws from the two end-member phases weighted by the fraction of each phase present (Huet et al., 2014; Ji, 2004; Ji et al., 2003; Tullis et al., 1991). The maximum and minimum bounds on the strength of a two-phase material are based on the assumptions of uniform-strain rate (Taylor, 1938) and uniform-stress (Sachs, 1928), respectively, between the two mineral phases. In Figure 5, the stress at the beginning and end of each experiment is plotted versus f_{Per}, along with the uniform-strain rate and uniform-stress bounds.

The uniform-strain rate and uniform-stress boundaries were calculated using the flow laws for the dominate deformation mechanism in each phase determined in Section 4.2, namely, disGBS for Ol (Hansen et al., 2011) and dislocation creep for Per_{100} (Equation 2) or dislocation creep for Per_{80} (Stretton et al., 2001). As discussed in Section 4.1.2, these end-member flow laws were scaled to account for the effect of differing Fe content on the mechanical behavior of each phase. This correction was carried out separately for each sample using the Fe content in Ol and Per appropriate to that sample. Recall that, as discussed in Section 4.1.4, silica activity does not significantly influence the strength Ol in the disGBS regime.

4.3.1. Small Strain Behavior

At small strains ($0 < \gamma < 1$) in Figure 5a, the stresses measured for samples with $0.7 \leq f_{Per} < 1.0$ align with the values predicted from the uniform-stress (lower) bound. As f_{Per} decreases to $0.5 \leq f_{Per} \leq 0.6$, stress falls between the two bounds but is still closer to that predicted from the uniform-stress (lower) bound. Finally, for samples with $f_{Per} \leq 0.5$, the measured stresses are greater than those predicted by the uniform-strain rate (upper) bound; samples with $f_{Per} = 0.1$ and 0.3 have strengths more than 20 MPa greater than those predicted by the uniform-strain rate (upper) bound. Similar observations were made by Ji et al. (2001) for small-strain ($\gamma < 0.5$) experiments on forsterite (Fo) + enstatite (En) for which Fo deformed via diffusion creep and En deformed via dislocation creep; in their study, the strengths of Fo-rich samples followed the uniform-stress boundary, and the strengths of En-rich samples followed the uniform-strain rate boundary. These authors described the change in sample strength from Fo-rich samples to En-rich samples as a change from a strong-phase supported, or load-bearing framework, regime to a weak-phase supported, or interconnected weak layer, regime (Handy, 1990; Ji et al., 2003). The samples in

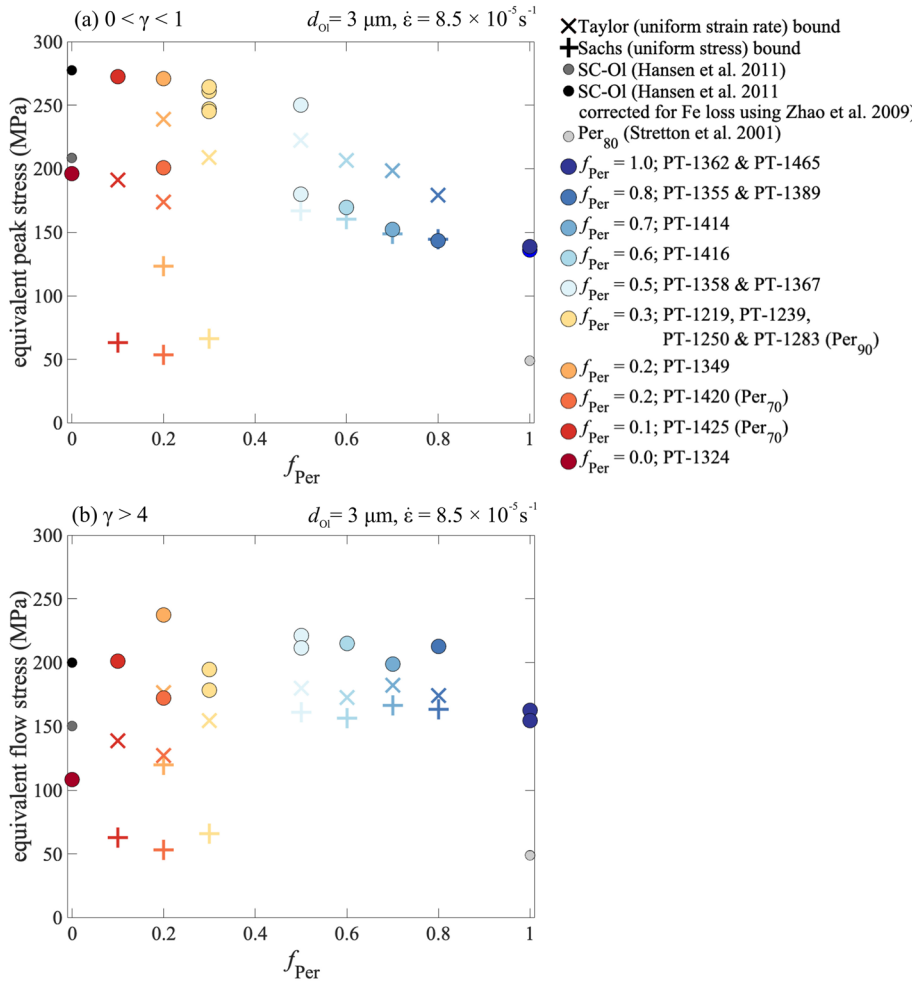

Figure 5. (a) Peak stress or stress at $0 < \gamma < 1$ versus f_{Per}, and (b) flow stress or stress at $\gamma > 4$ versus f_{Per}. In each panel, the theoretical predictions for the strength of a two-phase material based on assumptions of uniform-stress (Sachs, 1928) and uniform-strain rate (Taylor, 1938) are plotted as the minimum and maximum bounds on the strength, respectively. The Sachs and Taylor bounds were calculated for each sample composition based on the Fe content of Ol and Per in that sample. The + and × symbols represent the Sachs and Taylor bounds, respectively. Plotted for comparison are the values of stress predicted by the disGBS flow law for Ol for Fo_{90} (medium-gray circles) and Fo_{95} (dark-gray circles) (Hansen et al., 2011; Qi et al., 2021; Zhao et al., 2009) both without (a) and with (b) geometric softening observed at large strains in single-phase samples (Hansen et al., 2012). Additionally, the stress predicted by the dislocation creep flow law for Per_{80} is plotted on each subfigure (light-gray circle). Data from flow laws were calculated at an outer-radius equivalent strain rate of $\dot{\varepsilon} = 8.5 \times 10^{-5}$ s^{-1}, Ol grain size of $d_{Ol} = 3$ μm, $T = 1523$ K, and $P = 300$ MPa.

our study can be described similarly at small strains; Ol-rich ($f_{Per} < 0.5$) samples are strong-phase supported and Per-rich ($f_{Per} > 0.5$) samples are weak-phase supported. The calculated stress exponents in Figure 3 support this interpretation as the values of n for samples with $f_{Per} < 0.5$ are similar to that for single-phase Ol and values of n for samples with $f_{Per} > 0.5$ are similar to that for single-phase Per. In addition, the evolution of n with increasing f_{Per} does not follow the trend for n predicted by a rule of mixtures (Tullis et al., 1991) and is instead controlled by the dominant phase in each sample.

The difference between the strengths of our samples and the uniform-strain rate bound indicates the influence of another physical mechanism not accounted for in using the rule-of-mixtures approach. One hypothesis for the large strengths of our samples compared to the uniform-strain rate boundary is related to the presence of phase boundaries. There is some precedent for hardening associated with phase boundaries, both theoretically and experimentally. Ashby (1972) and Gittus et al. (1978) argued that, due to lattice and chemical mismatch across a phase boundary, glide and climb of dislocations along phase boundaries is more difficult than along grain

boundaries. Additionally, Wang et al. (2018) found that incoherent phase boundaries in their two-phase metallic alloy make it difficult for dislocation pileups to dissipate via climb into phase boundaries, resulting in samples with higher strengths than in samples without phase boundaries. Such situations could account for the higher overall strengths of our samples.

4.3.2. Large Strain Behavior

At large strain ($\gamma > 4$), the flow law for disGBS in Ol, adjusted to account for geometric weakening that occurs at large strains, predicts a strength similar to that for our dislocation creep flow law for Per_{100}. As a result, the uniform-stress and uniform-strain rate boundaries overlap one another for samples with $f_{Per} \geq 0.5$. For samples with $f_{Per} \leq 0.3$, wherein Per has larger Fe content than in samples with $f_{Per} \geq 0.5$, the two bounds are separated due to the significant decrease in strength of Per with increasing Fe content. However, in Figure 5b, nearly all the two-phase samples are stronger than either single-phase end-member and are therefore stronger than either the uniform-stress or the uniform-strain rate boundary.

4.3.3. Comparison to Other Two-Phase Materials and the Effect of Secondary Phases on Sample Strength

Recent high-strain experimental studies of two-phase, olivine-bearing materials have reported notably different mechanical behavior among their respective samples. As summarized here and in Section 1, these differences seem to correspond to the different mineralogy of the two-phase samples investigated: Bystricky et al. (2006) deformed aggregates of Ol + Per_{70} with $f_{Per} = 0.8$ in torsion to $\gamma = 14.9$ and observed strengths similar to single-phase Per_{70}. Tasaka et al. (2017, 2020) deformed aggregates of Fe-rich Ol + Opx with $f_{Opx} = 0.15$, 0.26, and 0.35 in torsion to $\gamma = 26.2$ and found that their samples were stronger than single-phase Fo_{50} at small strains but weakened with increasing strain. Sundberg and Cooper (2008) deformed aggregates of Ol + Opx with $f_{Opx} = 0.65$, 0.5, and 0.35 in general shear to $\gamma = 4$ and determined that their samples were weaker than the single-phase Ol end-member deformed under similar conditions. Finally, Zhao et al. (2019) deformed aggregates of Ol + Cpx with $f_{Cpx} = 0.5$ in general shear to $\gamma = 3.5$ and observed that their samples were significantly weaker than either single-phase end-member. Additionally, the results from our experiments on Ol + Per demonstrate another behavior in which Ol-rich samples have strengths greater than that of either single-phase end-member. Such differences between studies make it difficult to form generalizations about the behavior of two-phase samples and likely represent fundamental differences is the underlying physical processes occurring within each type of sample. To explain these differences and demonstrate the range of behaviors exhibited by two-phase materials, we compare our results to each of these previous studies on different two-phase systems below.

For Per-rich samples, Bystricky et al. (2006) found that the strengths of their two-phase samples of SC-Ol + Per_{70} with $f_{Per} = 0.8$ deformed to high strains at $T = 1300$ K were similar to those measured in experiments performed on single-phase Per_{70}. Our sample composed of SC-Ol + Per_{100} with $f_{Per} = 0.8$ displayed a similar result in that the strength of our sample matches the prediction from the uniform-stress bound. We also note that both the strength of the sample with $f_{Per} = 0.8$ and the strength predicted by the uniform-stress bound at $f_{Per} = 0.8$ are similar to that of Per_{100}. These observations indicate that the most Per-rich samples ($f_{Per} \geq 0.8$) may be less affected by the presence of a second phase than those with smaller Per-contents.

For Ol-rich samples, Tasaka et al. (2017, 2020) reported that their two-phase mixtures of Fo_{50} + En_{55} were stronger than single-phase Fo_{50} at small strains. As deformation continued to shear strains of $\gamma \gtrsim 20$, their samples strain weakened for the duration of the experiment, whereas samples of single-phase Fo_{50} did not strain weaken beyond $\gamma = 7$ (Hansen et al., 2012). Although the mechanical behavior of their two-phase samples is similar to that observed for our samples, they attributed the difference in strength at small strains to the fact that En is stronger than Ol. Unfortunately, this explanation does not hold for our samples of Ol + Per because Per is weaker than Ol at small strains and the two phases are of similar strengths at large strains. Consequently, an additional mechanism is required to explain the large sample strengths in the present study. The possibilities for strengthening discussed previously in Section 4.2.1 apply here, which are related to the nature of phase boundaries in our samples, as discussed further at the end of this section.

In contrast to the results of Tasaka et al. (2017, 2020), Sundberg and Cooper (2008) observed that their samples of Balsam Gap Ol (Fo_{92}) + Bamble Opx (En_{88}) with $f_{Opx} = 0.35$, 0.5, and 0.65 were weaker than single-phase Ol (Fo_{90}). Tasaka et al. (2017) pointed out several important differences between their results and those of Sundberg and Cooper (2008). These differences also apply to the results of this study, namely, a lack of solute

drag in our samples compared to the samples from Sundberg and Cooper (2008), deformation occurring via dislocation-accommodated interface sliding in our samples rather than interface-reaction limited diffusion creep in Sundberg and Cooper (2008), and experiments performed at higher stresses (>100 MPa) than in Sundberg and Cooper (2008) (<50 MPa). The presence of solutes and impurities in our samples will be addressed further below.

Similarly, for Cpx-bearing samples, Zhao et al. (2019) observed that their samples composed of 50:50 mixtures of SC-Ol + Damaping Cpx (Cpx_{91}) were much weaker than either single-phase end-member. They attributed this behavior to faster rates of diffusion along phase boundaries than along grain boundaries, resulting in enhanced sliding along the interfaces between grains of the two phases. Rather than being accommodated by dislocation motion, interfacial sliding in their case was accommodated by diffusion and rate-limited by interface reactions. This result for the Ol + Cpx system differs significantly from our results for Ol + Per materials in which our two-phase samples were stronger than their single-phase counterparts. Yet, as Zhao et al. (2019) did for their samples of Ol + Cpx, we argue that the distinction between the strength of our Ol + Per samples and the strength of the single-phase end-members is associated with the presence and properties of phase boundaries.

The difference in the role of phase boundaries between our samples and those of Zhao et al. (2019) are primarily due to the observation that interface sliding was dislocation-accommodated in our samples of Ol + Per but diffusion-accommodated in their samples of Ol + Cpx. Zhao et al. (2019) argued that diffusion may be much more rapid along phase boundaries than grain boundaries, at least in the Ol + Cpx system. However, as discussed in Section 4.2.1, Ashby (1972) and Gittus et al. (1978) argued that the motion of dislocations is more difficult along phase boundaries than along grain boundaries due to lattice and chemical mismatch and the resulting disordered structure at phase boundaries. Because deformation was dislocation-mediated in our samples, it is possible that phase boundaries contributed to our increased sample strength. Additionally, the use of high-purity Per as a second phase in our experiments reduces the concentration of grain-boundary impurities, such as Al and Ca, as well as the possibility of a small amount of melt compared to samples synthesized with naturally occurring Cpx or Opx as a secondary phase where such grain-boundary impurities and melt may be present. Per grain boundaries and grain interiors will take up a significant fraction of these impurities that are present in natural SC-Ol, likely forming Mg-silicates instead of melt and reducing the concentration of impurities along olivine grain boundaries. A decrease in the concentration of such grain-boundary impurities will also increase the strength of our two-phase samples relative to the end-member counterparts (Yabe & Hiraga, 2020; Yabe et al., 2020).

5. Conclusions

1. In our two-phase samples, deformation of Ol is dominated by dislocation-accommodated sliding along interfaces, while deformation of Per is dominated by dislocation creep.
   a) In Ol-rich samples, some strain weakening occurs between $0.5 < \gamma < 7.0$ due to a small amount of grain-size reduction and weak CPO development.
   b) In Per-rich samples, strain hardening occurs throughout the experiment, which we hypothesize due to the restriction of dislocation motion through interactions with dislocation pileups at phase boundaries and/or immobile dislocation.
2. At small strains, Ol-rich samples have strengths greater than the uniform-strain rate boundary and Per-rich samples have strengths similar to those predicted by the uniform-stress boundary (lower bound).
3. At large strains, our two-phase samples are stronger than predicted by a rule of mixtures based on the end-member flow laws, i.e., the uniform-strain rate boundary (upper bound). This behavior is likely due to the presence of phase boundaries in our samples and their interactions with dislocations during deformation.

Data Availability Statement

All data used in this study are available from the University of Minnesota Digital Conservancy (https://doi.org/10.13020/k0p0-5047, Wiesman et al., 2023).

Acknowledgments
We would like to thank Amanda Dillman, Lars Hansen, Leïla Hashim, Cameron Meyers, Zachary Michels, Chao Qi, and Amy Ryan for many invaluable discussions. The authors are also grateful to Anette van der Handt for her expertise and help with electron microprobe analyses. This manuscript was improved by thoughtful comments and reviews from Takehiko Hiraga and David Bercovici. This research was funded by NSF Grants EAR-1755498 (M.E.Z.) and EAR-1755805 (D.L.K.). Parts of this work were carried out in the Characterization Facility, University of Minnesota, which receives partial support from the NSF through the MRSEC (Award DMR-2011401) and the NNCI (Award ECCS-2025124) programs. Electron microprobe analyses were carried out at the Electron Microprobe Laboratory, University of Minnesota, Department of Earth and Environmental Sciences, University of Minnesota-Twin Cities.

References

Ambrose, T. K., Wallis, D., Hansen, L. N., Waters, D. J., & Searle, M. P. (2018). Controls on the rheological properties of peridotite at a palaeo-subduction interface: A transect across the base of the Oman-UAE ophiolite. *Earth and Planetary Science Letters*, *491*, 193–206. https://doi.org/10.1016/j.epsl.2018.03.027

Ashby, M. F. (1972). Boundary defects, and atomistic aspects of boundary sliding and diffusional creep. *Surface Science*, *31*, 498–542. https://doi.org/10.1016/0039-6028(72)90273-7

Bai, Q., Mackwell, S. J., & Kohlstedt, D. L. (1991). High-temperature creep of olivine single crystals 1: Mechanical results for buffered samples. *Journal of Geophysical Research*, *96*(B2), 2441–2463. https://doi.org/10.1029/90JB01723

Bercovici, D., & Mulyukova, E. (2018). A continuum theory for phase mixing and grain-damage relevant to tectonic plate boundary evolution. *Physics of the Earth and Planetary Interiors*, *285*, 23–44. https://doi.org/10.1016/j.pepi.2018.10.005

Bercovici, D., & Mulyukova, E. (2021). Evolution and demise of passive margins through grain mixing and damage. *Proceedings of the National Academy of Sciences of the United States of America*, *118*(4), e2011247118. https://doi.org/10.1073/pnas.2011247118

Bercovici, D., Mulyukova, E., Girard, J., & Skemer, P. (2023). A coupled model for phase mixing, grain damage and shear localization in the lithosphere: Comparison to lab experiments. *Geophysical Journal International*, *232*(3), 2205–2230. https://doi.org/10.1093/gji/ggac428

Bercovici, D., & Ricard, Y. (2012). Mechanisms for the generation of plate tectonics by two-phase grain-damage and pinning. *Physics of the Earth and Planetary Interiors*, *202–203*, 27–55. https://doi.org/10.1016/j.pepi.2012.05.003

Bilde-Sörensen, J. B. (1972). Dislocation structures in creep-deformed polycrystalline MgO. *Journal of the American Ceramic Society*, *55*(12), 606–610. https://doi.org/10.1111/j.1151-2916.1972.tb13453.x

Bystricky, M., Heidelbach, F., & Mackwell, S. (2006). Large-strain deformation and strain partitioning in polyphase rocks: Dislocation creep of olivine-magnesiowüstite aggregates. *Tectonophysics*, *427*(1–4), 115–132. https://doi.org/10.1016/j.tecto.2006.05.025

Czertowicz, T. A., Toy, V. G., & Scott, J. M. (2016). Recrystallisation, phase mixing and strain localisation in peridotite during rapid extrusion of sub-arc mantle lithosphere. *Journal of Structural Geology*, *88*, 1–19. https://doi.org/10.1016/j.jsg.2016.04.011

Evans, B., Renner, J., & Hirth, G. (2001). A few remarks on the kinetics of static grain growth in rocks. *International Journal of Earth Sciences*, *90*(1), 88–103. https://doi.org/10.1007/s005310000150

Frost, H., & Ashby, M. (1982). *Deformation mechanism maps*. Pergamon.

Gittus, J. H., Cook, A. H., Poirier, J. P., Murrell, S. A. F., & Weertman, J. (1978). High-temperature deformation of two phase structures. *Philosophical Transactions of the Royal Society of London-Series A: Mathematical and Physical Sciences*, *288*, 121–146. http://www.jstor.org/stable/74979

Goddard, R. M., Hansen, L. N., Wallis, D., Stipp, M., Holyoke, C. W., III, Kumamoto, K. M., & Kohlstedt, D. L. (2020). A subgrain-size piezometer calibrated for EBSD. *Geophysical Research Letters*, *47*, e2020GL090056. https://doi.org/10.1029/2020GL090056

Handy, M. R. (1990). The solid-state flow of polymineralic rocks. *Journal of Geophysical Research*, *95*(B6), 8647–8661. https://doi.org/10.1029/JB095iB06p08647

Hansen, L. N., & Warren, J. M. (2015). Quantifying the effect of pyroxene on deformation of peridotite in a natural shear zone. *Journal of Geophysical Research: Solid Earth*, *120*, 2717–2738. https://doi.org/10.1002/2014JB011584

Hansen, L. N., Zimmerman, M. E., & Kohlstedt, D. L. (2011). Grain boundary sliding in San Carlos olivine: Flow law parameters and crystallographic-preferred orientation. *Journal of Geophysical Research*, *116*, B08201. https://doi.org/10.1029/2011JB008220

Hansen, L. N., Zimmerman, M. E., & Kohlstedt, D. L. (2012). The influence of microstructure on deformation of olivine in the grain-boundary sliding regime. *Journal of Geophysical Research*, *117*, B09201. https://doi.org/10.1029/2012JB009305

Heidelbach, F., Stretton, I., Langenhorst, F., & Mackwell, S. (2003). Fabric evolution during high strain shear deformation of magnesiowüstite ($Mg_{0.8}Fe_{0.2}O$). *Journal of Geophysical Research*, *108*(B3), 2154. https://doi.org/10.1029/2001JB001632

Heidelbach, F., Terry, M. P., Bystricky, M., Holzapfel, C., & McCammon, C. (2009). A simultaneous deformation and diffusion experiment: Quantifying the role of deformation in enhancing metamorphic reactions. *Earth and Planetary Science Letters*, *278*(3–4), 386–394. https://doi.org/10.1016/j.epsl.2008.12.026

Hensler, J. H., & Cullen, G. V. (1968). Stress, temperature, and strain rate in creep of magnesium oxide. *Journal of the American Ceramic Society*, *51*(10), 557–559. https://doi.org/10.1111/j.1151-2916.1968.tb13321.x

Herwegh, M., Linckens, J., Ebert, A., Berger, A., & Brodhag, S. H. (2011). The role of second phases for controlling microstructural evolution in polymineralic rocks: A review. *Journal of Structural Geology*, *33*(12), 1728–1750. https://doi.org/10.1016/j.jsg.2011.08.011

Hirth, G., & Kohlstedt, D. (2003). Rheology of the mantle wedge. In J. Eiler (Ed.), *Inside the subduction factory*. *Geophysical monograph series* (Vol. 138, pp. 83–105). American Geophysical Union.

Huet, B., Yamato, P., & Grasemann, B. (2014). The minimized power geometric model: An analytical mixing model for calculating polyphase rock viscosities consistent with experimental data. *Journal of Geophysical Research: Solid Earth*, *119*, 3897–3924. https://doi.org/10.1002/2013JB010453

Ji, S. (2004). A generalized mixture rule for estimating the viscosity of solid-liquid suspensions and mechanical properties of polyphase rocks and composite materials. *Journal of Geophysical Research*, *109*, B10207. https://doi.org/10.1029/2004JB003124

Ji, S., Zhao, P., & Xia, B. (2003). Flow laws of multiphase materials and rocks from end-member flow laws. *Tectonophysics*, *370*(1–4), 129–145. https://doi.org/10.1016/S0040-1951(03)00182-3

Ji, S. C., Wang, Z. C., & Wirth, R. (2001). Bulk flow strength of forsterite—Enstatite composites as a function of forsterite content. *Tectonophysics*, *341*(1–4), 69–93. https://doi.org/10.1016/s0040-1951(01)00191-3

Langdon, T. G. (2006). Grain boundary sliding revisited: Developments in sliding over four decades. *Journal of Material Science*, *41*(3), 597–609. https://doi.org/10.1007/s10853-006-6476-0

Langdon, T. G., & Pask, J. A. (1970). The mechanism of creep in polycrystalline magnesium oxide. *Acta Metallurgica*, *18*(5), 505–510. https://doi.org/10.1016/0001-6160(70)90137-9

Linckens, J., Herwegh, M., Muntener, O., & Mercolli, I. (2011). Evolution of a polymineralic mantle shear zone and the role of second phases on the localization of deformation. *Journal of Geophysical Research*, *116*, B06210. https://doi.org/10.1029/2010JB008119

Manohar, P. A., Ferry, M., & Chandra, T. (1998). Five decades of the Zener equation. *ISIJ International*, *38*(9), 913–924. https://doi.org/10.2355/isijinternational.38.913

Meyers, C. D., Kohlstedt, D. L., & Zimmerman, M. E. (2017). *Densification and grain growth in polycrystalline olivine rocks synthesized by evacuated hot-pressing*. AGU Fall Meeting Abstracts 2017, MR23A-07.

Nakakoji, T., Hiraga, T., Nagao, H., Ito, S., & Kano, M. (2018). Diffusion creep and grain growth in forsterite +20 vol% enstatite aggregates: 1. High-resolution experiments and their data analyses. *Journal of Geophysical Research: Solid Earth*, *123*, 9486–9512. https://doi.org/10.1029/2018JB015818

Okamoto, A., & Hiraga, T. (2022). A common diffusional mechanism for creep and grain growth in polymineralic rocks: Experiments. *Journal of Geophysical Research: Solid Earth*, *127*, e2022JB024638. https://doi.org/10.1029/2022JB024638

Paterson, M., & Olgaard, D. (2000). Rock deformation tests to large shear strains in torsion. *Journal of Structural Geology*, *22*(9), 1341–1358. https://doi.org/10.1016/S0191-8141(00)00042-0

Paterson, M. S. (1990). Rock deformation experimentation. In A. G. Duba, & W. B. Durham (Eds.), *The brittle ductile transition in rocks, the heard volume*. *Geophysical monograph series* (Vol. 56, pp. 187–194). American Geophysical Union.

Qi, C., Zhao, Y.-H., Zimmerman, M. E., Kim, D., & Kohlstedt, D. L. (2021). Evolution of microstructural properties in sheared iron-rich olivine. *Journal of Geophysical Research: Solid Earth*, *126*, e2020JB019629. https://doi.org/10.1029/2020JB019629

Ricoult, D. L., & Kohlstedt, D. L. (1985). Experimental evidence for the effect of chemical environment upon the creep rate of olivine. In R. N. Schock (Ed.), *Point defects in minerals*. https://doi.org/10.1029/GM031p0171

Rollett, A. D., & Kocks, U. F. (1993). A review of the stages of work hardening. *Solid State Phenomena*, *35*(36), 1–18. https://doi.org/10.4028/www.scientific.net/ssp.35-36.1

Rollett, A. D., Kocks, U. F., Embury, J. D., Stout, M. G., & Doherty, R. D. (1988). Strain hardening at large strains. In *International conference on strength of metals and alloys*.

Sachs, G. (1928). Zur ableitung einer fliessbedingung. *Zeitschrift des Vereines Deutscher Ingenieure*, *72*, 734–736.

Smith, C. S. (1948). Grains, phases, interfaces: An interpretation of microstructures. *Transactions of the American Institute of Mining and Metallurgical Engineers*, *175*, 15–51.

Stretton, I., Heidelbach, F., Mackwell, S., & Langenhorst, F. (2001). Dislocation creep of magneseowüstite ($Mg_{0.8}Fe_{0.2}O$). *Earth and Planetary Science Letters*, *196*(1–2), 229–240. https://doi.org/10.1016/s0012-821x(01)00533-7

Sundberg, M., & Cooper, R. F. (2008). Crystallographic preferred orientation produced by diffusional creep of harzburgite: Effects of chemical interactions among phases during plastic flow. *Journal of Geophysical Research*, *113*, B12208. https://doi.org/10.1029/2008JB005618

Tasaka, M., Hiraga, T., & Michibayashi, K. (2014). Influence of mineral fraction on the rheological properties of forsterite + enstatite during grain size sensitive creep: 3. Application of grain growth and flow laws on peridotite ultramylonites. *Journal of Geophysical Research: Solid Earth*, *119*, 840–857. https://doi.org/10.1002/2013JB010619

Tasaka, M., & Hiraga, T. (2013). Influence of mineral fraction on the rheological properties of forsterite + enstatite during grain size sensitive creep: 2. Deformation experiments. *Journal of Geophysical Research: Solid Earth*, *118*, 3991–4012. https://doi.org/10.1002/jgrb.50284

Tasaka, M., Zimmerman, M. E., & Kohlstedt, D. L. (2017). Rheological weakening of olivine + orthopyroxene aggregates due to phase mixing: 1. Mechanical behavior. *Journal of Geophysical Research: Solid Earth*, *122*, 7584–7596. https://doi.org/10.1002/2017JB014333

Tasaka, M., Zimmerman, M. E., & Kohlstedt, D. L. (2020). Rheological weakening of olivine + orthopyroxene aggregates due to phase mixing: Effects of orthopyroxene volume fraction. *Journal of Geophysical Research: Solid Earth*, *125*, e2020JB019888. https://doi.org/10.1029/2020JB019888

Taylor, G. I. (1938). Plastic strain in metals. *Journal of the Institute of Metals*, *62*, 307–324.

Tullis, T. E., Horowitz, F. G., & Tullis, J. (1991). Flow laws of polyphase aggregates from end-member flow laws. *Journal of Geophysical Research*, *96*(B5), 8081–8096. https://doi.org/10.1029/90JB02491

von Mises, R. (1913). Mechanik der festen Körper im plastisch-deformablen Zustand. Nachrichten von der Gesellschaft der Wissenschaften zu Göttingen. *Mathematisch-Physikalische Klasse*, *1913*(1), 582–592.

Wang, Q., Lu, Y., Yu, Q., & Zhang, Z. (2018). The exceptional strong face-centered cubic phase and semi-coherent phase boundary in a eutectic dual-phase high entropy alloy AlCoCrFeNi. *Scientific Reports*, *8*(1), 14910. https://doi.org/10.1038/s41598-018-33330-0

Wang, Z., Zhao, Y., & Kohlstedt, D. L. (2010). Dislocation creep accommodated by grain boundary sliding in dunite. *Journal of Earth Sciences*, *21*(5), 541–554. https://doi.org/10.1007/s12583-010-0113-1

Warren, J. M., & Hirth, G. (2006). Grain size sensitive deformation mechanisms in naturally deformed peridotites. *Earth and Planetary Science Letters*, *248*(1–2), 438–450. https://doi.org/10.1016/j.epsl.2006.06.006

Wenk, H. R., Bennett, K., Canova, G. R., & Molinari, A. (1991). Modeling plastic deformation of peridotite with the self-consistent theory. *Journal of Geophysical Research*, *96*(B5), 8337–8349. https://doi.org/10.1029/91JB00117

Wiesman, H. S., Zimmerman, M. E., & Kohlstedt, D. L. (2018). Laboratory investigation of mechanisms for phase mixing in olivine + ferropericlase aggregates. *Philosophical Transactions of the Royal Society A*, *376*(2132), 20170417. https://doi.org/10.1098/rsta.2017.0417

Wiesman, H. S., Zimmerman, M. E., & Kohlstedt, D. L. (2023). The effect of secondary-phase fraction on the deformation of olivine + ferropericlase aggregates: 1. Microstructural evolution. *Journal of Geophysical Research: Solid Earth*. https://doi.org/10.1029/2022JB025723

Yabe, K., & Hiraga, T. (2020). Grain- boundary diffusion creep of olivine: 2. Solidus effects and consequences for the viscosity of the oceanic upper mantle. *Journal of Geophysical Research: Solid Earth*, *125*, e2020JB019416. https://doi.org/10.1029/2020JB019416

Yabe, K., Sueyoshi, K., & Hiraga, T. (2020). Grain-boundary diffusion creep of olivine: 1. Experiments at 1 atm. *Journal of Geophysical Research: Solid Earth*, *125*, e2020JB019415. https://doi.org/10.1029/2020JB019415

Zehetbauer, M., Stüwe, H., Vorhauer, A., Schafler, E., & Kohout, J. (2003). The role of hydrostatic pressure in severe plastic deformation. *Advanced Engineering Materials*, *5*, 330–337. https://doi.org/10.1002/adem.200310090

Zehetbauer, M. J. (2000). Strengthening processes of metals by severe plastic deformation. In T. C. Lowe, & R. Z. Valiev (Eds.), *Investigations and applications of severe plastic deformation. NATO science series (series 3. High technology)* (Vol. 80). Springer. https://doi.org/10.1007/978-94-011-4062-1_11

Zhao, N., Hirth, G., Cooper, R. F., Kruckenberg, S. C., & Cukjati, J. (2019). Low viscosity of mantle rocks linked to phase boundary sliding. *Earth and Planetary Science Letters*, *517*, 83–94. https://doi.org/10.1016/j.epsl.2019.04.019

Zhao, Y.-H., Zimmerman, M. E., & Kohlstedt, D. L. (2009). Effect of iron content on the creep behavior of olivine: 1. Anhydrous conditions. *Earth and Planetary Science Letters*, *287*(1–2), 229–240. https://doi.org/10.1016/j.epsl.2009.08.006